Sensitivity of modeled arctic mixed-phase stratocumulus to cloud condensation and ice nuclei over regionally varying surface conditions

Hugh Morrison,[1] James O. Pinto,[1] Judith A. Curry,[2] and Greg M. McFarquhar[3]

Received 29 March 2007; revised 22 September 2007; accepted 4 December 2007; published 4 March 2008.

[1] A two-moment microphysics scheme implemented in the polar version of the mesoscale model MM5 is used to simulate a mixed-phase stratocumulus deck observed during the Fall 2004 Mixed-Phase Arctic Cloud Experiment (MPACE). In situ aircraft instrumentation and remote sensors gathered extensive microphysical and radiative data that serve as a testbed for the model. Model results are reasonably similar to observations in terms of the liquid microphysical properties, while the ice microphysical properties are more significantly biased, especially the ice crystal concentration. Sensitivity tests examine the impact of increased cloud condensation and ice nucleus concentrations. Increasing the concentration of cloud condensation nuclei to values typical for polluted 'Arctic haze' conditions substantially reduces the mean droplet size, but has little impact on the downwelling longwave flux because the cloud already emits as a blackbody (except near the Arctic Ocean pack ice edge). However, the smaller droplet size does lead to a slight increase in liquid water path and more significant decrease ($\sim$50%) in the ice water path and snowfall rate due to reduced collision-coalescence and riming of snow by droplets. Increasing the ice nucleus concentration specified from MPACE observations by 1–2 orders of magnitude produces a substantial reduction in liquid water path and downwelling longwave flux at the surface over interior northern Alaska, but has less impact over the open ocean and coastal regions. However, a large discrepancy between the observed ice nucleus and ice crystal concentrations, leading to the underprediction of simulated crystal concentration, also suggests that additional ice initiation mechanisms (not included in current models) may have occurred in the real cloud layer.

Citation: Morrison, H., J. O. Pinto, J. A. Curry, and G. M. McFarquhar (2008), Sensitivity of modeled arctic mixed-phase stratocumulus to cloud condensation and ice nuclei over regionally varying surface conditions, *J. Geophys. Res.*, *113*, D05203, doi:10.1029/2007JD008729.

1. Introduction

[2] Clouds and their impact on the transfer of longwave and solar radiation are among the most challenging aspect of simulating present-day climate and, more importantly, climate change [e.g., *Stephens*, 2005 and references therein]. One of the most uncertain aspects of climate-cloud interactions is the indirect effect atmospheric aerosols have on the radiation budget by influencing the microphysical and macrophysical properties of clouds. The first aerosol indirect effect concerns the influence of aerosols on droplet size and hence cloud optical depth [e.g., *Twomey*, 1977] and emissivity [e.g., *Lubin and Vogelmann*, 2006] for a given liquid water path. It has also been hypothesized that smaller droplets could reduce precipitation efficiency, increasing the longevity and water content of the cloud, i.e., the second indirect effect [e.g., *Albrecht*, 1989]. Despite the recent emphasis of observational and modeling studies on indirect aerosol effects, few studies have focused specifically on indirect aerosol effects in the Arctic.

[3] Indirect aerosol effects may differ significantly in the Arctic compared with other regions due to uniqueness of the surface and thermodynamic properties of the atmosphere. Low-level mixed-phase clouds tend to occur frequently throughout the year [e.g., *Intrieri et al.*, 2002; *Pinto et al.*, 2001; *Morrison et al.*, 2005c]. These clouds may be especially sensitive to aerosol since they are colloidally unstable and tend to occur under weak synoptic forcing [*Curry et al.*, 2000; *Zuidema et al.*, 2005]. Indirect aerosol effects may be particularly important over the Arctic Ocean, since fairly small changes in the surface radiative fluxes may significantly impact the thickness and concentration of sea ice over climatic timescales [*Curry and Ebert*, 1990; *Curry et al.*, 1993]. These surface changes may, in turn, impact the aerosol and cloud microphysics, representing a potentially important feedback pathway. Understanding these interactions and feedbacks is critical since climate modeling results have highlighted the Arctic as a region of

[1] National Center for Atmospheric Research, Boulder, Colorado, USA.
[2] School of Earth and Atmospheric Science, Georgia Institute of Technology, Atlanta, Georgia, USA.
[3] University of Illinois, Urbana, Illinois, USA.

0148-0227/08/2007JD008729$09.00

particular vulnerability to global climate change [*Houghton et al.*, 2001].

[4] Arctic aerosols have a distinct annual cycle with pristine conditions in late summer and polluted conditions common during winter and spring [e.g., *Barrie*, 1986; *Curry*, 1995; *Sirois and Barrie*, 1999]. Arctic pollution aerosols ('arctic haze') are associated with long-range transport from the midlatitudes of the North American and Eurasian continents. It has been suggested that arctic pollution aerosol may modify the characteristics of cloud condensation nuclei (CCN) and thus droplet number concentration and size [e.g., *Shaw*, 1986; *Curry*, 1995; *Curry et al.*, 1996; *Garrett et al.*, 2002; *Lubin and Vogelmann*, 2006].

[5] Recent studies by *Garrett et al.* [2002], *Garrett and Zhou* [2006], and *Lubin and Vogelmann* [2006] suggest the particular importance of indirect aerosol effects on the longwave radiative fluxes in the Arctic, while most global and lower latitude studies have focused on shortwave indirect effects. At higher latitudes, longwave cloud radiative forcing dominates the net cloud radiative forcing throughout much of the year [*Shupe and Intrieri*, 2004]. Arctic clouds often have relatively low liquid water paths and hence tend to emit as graybodies, meaning that they are potentially susceptible to aerosol-induced changes in emissivity.

[6] Arctic pollution aerosol may also impact ice nucleation by modifying the characteristics of ice-forming nuclei (IN). However, aerosol-ice microphysical interactions, and their potential impact on the regional cloud cover, thermodynamics, and mesoscale dynamics in the Arctic, remain highly uncertain. The impact of pollution on IN is hypothesized to be largely dependent upon the chemical composition. *Borys* [1989] suggested that a large sulfate component may deactivate existing IN. Modeling studies suggest that the microphysical and macrophysical properties of Arctic mixed-phase clouds are highly sensitive to the assumed concentration of IN [*Pinto*, 1998; *Harrington et al.*, 1999; *Jiang et al.*, 2000; *Morrison et al.*, 2005b]. Specifically, increasing the IN concentration tends to produce rapid glaciation of the simulated mixed-phase clouds.

[7] Observations in midlatitudes have suggested that pollution decreases the snowfall rate due to increasing droplet number concentration and hence decreased droplet size and riming rate [*Borys et al.*, 2000, 2003]. The impact of pollution aerosols on arctic clouds is less clear due to lack of observations. *Lohmann et al.* [2003] suggest from modeling results that the riming rate in arctic clouds is sensitive to pollution aerosol, but they found that the impact on snowfall rate depended strongly on the assumed crystal shape.

[8] Two-moment bulk cloud microphysics schemes predicting both number concentration and mixing ratio of cloud water have been increasingly used in recent years to simulate indirect aerosol effects in cloud and climate models [e.g., *Ghan et al.*, 1997; *Lohmann et al.*, 1999; *Saleeby and Cotton*, 2004; *Morrison and Grabowski*, 2006]. The prediction of cloud particle number concentration provides a more physical treatment of aerosol indirect effects than using simpler one-moment schemes (i.e., schemes that predict cloud water mixing ratio only). Relevant parameters (e.g., effective radius) can be diagnosed from the predicted moments assuming some functional form for the particle size distributions (e.g., gamma, lognormal). While size-resolving (bin) microphysics models that explicitly calculate particle size distributions provide a more detailed solution, they are much more computationally expensive and still rely on a number of uncertain parameters, especially for the ice phase. It follows that bulk schemes are currently the only viable approach for many applications, especially for climate and weather prediction models that require a reasonable level of computational efficiency.

[9] In our previous work [*Morrison and Pinto*, 2005, 2006; hereafter MP05; MP06], a new two-moment bulk scheme was developed and incorporated into the polar version of the Fifth Generation Pennsylvania State University/NCAR Mesoscale Model MM5 [*Bromwich et al.*, 2001]. Model results were compared with observations of mixed-phase clouds obtained in May 1998 over the Arctic pack ice during the Surface Heat Budget of the Arctic Ocean (SHEBA) and First ISCCP Regional Experiment–Arctic Clouds Experiment (FIRE-ACE). The new scheme was able to simulate reasonably the persistence and microphysical characteristics of these clouds, but the lifetime and liquid water content were quite sensitive to several microphysical and thermodynamic parameters, especially the assumed IN concentration.

[10] In this study, we extend the work of MP05 and MP06 by applying the polar MM5 coupled with the MP05 two-moment microphysics scheme to simulate a mixed-phase cloud field observed during the Fall 2004 Mixed-Phase Arctic Clouds Experiment [MPACE; *Verlinde et al.*, 2007]. Conditions during MPACE differed substantially from SHEBA/FIRE-ACE, most notably by the surface conditions (i.e., open ocean rather than ice-covered). During MPACE, ground-based remote sensors and research aircraft were used to investigate mixed-phase cloud properties and processes along the Alaska North Slope and adjacent Arctic Ocean. The goals of this study are to evaluate the model's performance for the MPACE conditions, and quantify the sensitivity of the modeled cloud layer to concentrations of ice nuclei and cloud condensation nuclei. The indirect impacts of aerosol are examined in terms of the cloud microphysical and macrophysical properties, boundary layer structure, surface radiative fluxes, and mesoscale and large-scale dynamics. In addition, we examine how these model sensitivities vary according to the surface conditions, especially between the open ocean of the Beaufort Sea and the adjacent snow covered land of northern Alaska.

[11] The paper is organized as follows. In section 2 the instrumentation and observations are described and the case study is outlined. Section 3 gives an overview of the model description and details new upgrades to the two-moment microphysics scheme. Baseline model results are compared to observations in section 4, while section 5 describes sensitivity to aerosol properties. Summary and conclusions are given in section 6.

2. Observations

[12] During MPACE, which was conducted from late September through October 2004, ground-based and airborne sensors were used to characterize mixed-phase cloud microphysics, dynamics, and thermodynamics along the

Figure 1. Map of the MPACE domain and location of the four surface sites.

North Slope of Alaska and adjacent Arctic Ocean [*Verlinde et al.*, 2007]. MPACE was designed so that the ensuing data set could be used as a testbed to evaluate and improve the representation of Arctic mixed-phase clouds in climate and weather models.

2.1. Instrumentation

[13] The MPACE experimental domain consisted of four surface sites in northern Alaska: Barrow, Atqasuk, Oliktok Point, and Toolik Lake (Figure 1). The Department of Energy Atmospheric Radiation Measurement North Slope of Alaska site (ARM NSA) near Barrow (http://www.arm.gov/sites/nsa.stm) has hosted a suite of instruments since 1998, which was augmented by additional instrumentation during MPACE. The University of North Dakota Citation aircraft provided in situ measurements during the experiment. The Citation performed ascent and descent spirals near Barrow and Oliktok Point as well as porpoising and constant altitude legs between the two sites. In this study we use Citation data collected during the first two flights on October 9–10. In addition, the Aerosonde UAV [*Holland et al.*, 2001; *Curry et al.*, 2004] operated out of Barrow and provided in situ cloud, thermodynamic, and aerosol data. Near-surface aerosol data is provided by the NOAA Climate Monitoring and Diagnostic Laboratory (now Global Monitoring Division) located near the ARM NSA site at Barrow (http://www.cmdl.noaa.gov/obop/BRW/).

[14] This study utilizes data collected at the Barrow and Oliktok surface sites and in situ measurements from the Citation and Aerosonde UAV for model evaluation. Note that the following description is not a comprehensive listing of all the measurements available during MPACE, but rather gives an overview of the measurements of relevance to this study. Millimeter-Wavelength Cloud Radar, Micropulse Lidar, and laser ceilometers provide information on cloud boundaries and phase. Cloud liquid water path is derived from microwave radiometer measurements following *Turner et al.* [2006]. The longwave and shortwave radiative fluxes at the surface are derived from pyrgeometeor and pyranometer measurements that have been quality tested with the QCRad code [*Long and Shi*, 2006]. Broadband surface albedo is obtained from the upwelling and downwelling shortwave flux measurements. Accumulated precipitation at the surface was measured both at the National Weather Service (NWS) station as well as near the ARM NSA site in Barrow. Note that the observed precipitation is highly uncertain due to factors of the high-latitude environment (e.g., blowing snow, sublimation) [e.g., *Yang*, 1999], especially given the small precipitation amounts recorded during MPACE. This is reflected by the large difference in accumulated precipitation (about an order of magnitude) recorded at the NWS and ARM sites during the period.

[15] *McFarquhar et al.* [2007] describe the cloud physics instrumentation installed on the Citation and the processing techniques used to determine the bulk microphysical parameters needed to evaluate the model. The size distributions of the supercooled water droplets were determined from the FSSP (range of 3 to 53 μm) adjusted to match the bulk water content measured by the King probe and the one-dimensional cloud probe (1DC) when drizzle was present (see *McFarquhar et al.* [2007] for details). The ice crystal size distributions for particles larger than 53 μm were determined from the 1DC (53 to 125 μm), 2DC (125 to 1000 μm), and HVPS (1 to 40 mm) probes, or from the 2DC data extended by fits to larger sizes when the HVPS data were not available. Ice particles <53 μm were not included in the analysis shown here. There is some ambiguity in the interpretation of data from the 1DC and FSSP in mixed- and ice-phase conditions due to the possibility of shattering as well as difficulty in clearly separating water drops from spherical ice crystals, but since *McFarquhar et al.* [2007] determined that the majority of ice mass was contained in crystals larger than 1 mm, this uncertainty does not greatly affect the derived IWC used to compare against model simulations in this study, although it could impact estimates of concentration. Ice effective radius is calculated using the definition of *Fu* [1996]. Uncertainty associated with these estimates is detailed by *McFarquhar et al.* [2007].

[16] Data from the Met One Handheld Particle Counter (HHPC-6) measured the aerosol size distribution. The HHPC-6 is a 6 size-channel ($\sim$0.3 to 5 μm diameter with flow rate of 2.83 L/min) optical particle counter that was flown on the Aerosonde UAV. We use the five smallest size channels in this analysis given some uncertainty in sizing of the largest channel. Total aerosol concentration was measured with a condensation nucleus (CN) counter located at the NOAA CMDL near Barrow (see section 2.3). It assumed that the CMDL measurements are characteristic of aerosols throughout the domain.

2.2. Case Study Description

[17] During MPACE three distinct weather regimes were noted [*Verlinde et al.*, 2007]. This study focuses on the second regime, occurring between about 4 and 15 October. This period was characterized by strengthening high pressure over the pack ice region north of Alaska, bringing air from the pack ice, across the open Beaufort Sea, and onto the Alaskan coast with winds from the east to northeast. Figure 2 illustrates the synoptic situation that characterized the flow pattern over the Beaufort Sea and North Slope of Alaska on 9–10 October. The pack ice edge was located along the sharp temperature gradient seen across the north-

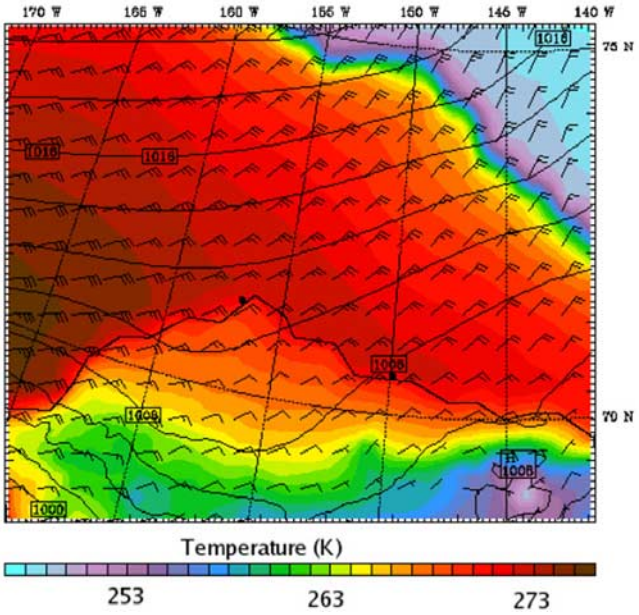

Figure 2. Eta analysis (interpolated to the 10 km MM5 Domain 2 grid) of surface air temperature (color contours), sea level pressure (black contours, interval of 2 mb), and near-surface winds (barbed vectors, full barb = 5 m s^{-1}), at 1200 UTC 10 October 2004. Barrow and Oliktok Point are indicated by black dots.

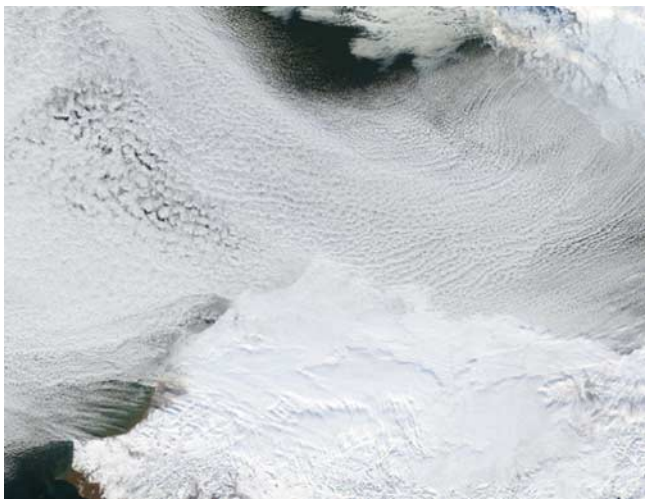

Figure 3. Composite visible image from the NASA Terra satellite for 9 October 2004.

eastern part of the domain shown in Figure 2. During this period, surface temperatures over the pack ice had dropped to ~−25°C according to National Center for Environmental Prediction (NCEP) Eta analyses. As this air traveled over the relatively warm open ocean, extensive boundary layer roll stratocumulus clouds developed (Figure 3). Note that the large-scale flow pattern and cloud field varied little during this period. The cloud top height at Barrow varied between 1–1.5 km with periodic oscillations. A persistent boundary layer cloud was also observed at Oliktok Point, although early on 9 October a second cloud layer was present above the boundary layer at ~2 km. Note that the boundary layer cloud top height at Oliktok Point tended to be somewhat lower than at Barrow during the latter part of Oct. 9 and early part of Oct. 10. The boundary layer near the coast was well-mixed from the surface to cloud top, with the cloud top temperature as cold as 257 K (Figure 4). An inversion of ~3 K was present just above the boundary layer. This cloud was mixed-phase, with liquid water dominant near cloud top and shafts of ice precipitation (and possibly some supercooled drizzle) present below the main cloud layer. Total water content and particle number concentration were dominated by the liquid hydrometeors through most of the cloud layer (see aircraft observations described in section 4).

2.3. Aerosol and Ice Nuclei Observations

[18] The (dry) aerosol size distribution is characterized by HHPC-6 measurements from the 10 October flight of the Aerosonde UAV, along with mean CN observations from the NOAA CMDL. Note that the in situ HHPC-6 data were taken below the cloud layer, with the 5 smallest size channels used here. A bimodal lognormal aerosol size distribution is fit to the HHPC-6 data and constrained so that the total concentration matches the CN measurements from the NOAA CMDL (Figure 5). The CN measurements are temporally averaged from 5–14 October; during this period the low-level flow field did not vary significantly (although locally varying aerosol properties are inferred from droplet concentration measurements, see section 4).

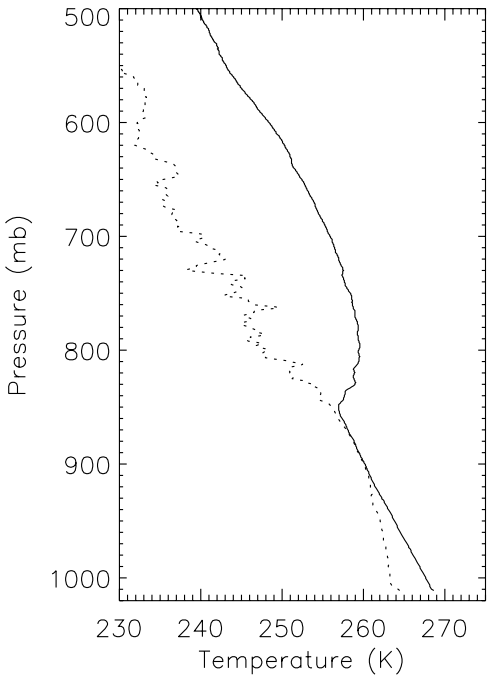

Figure 4. Observed dry-bulb (solid) and dew point (dotted) temperature profiles from the sounding launched at about 2300 UTC 9 October at the ARM facility near Barrow.

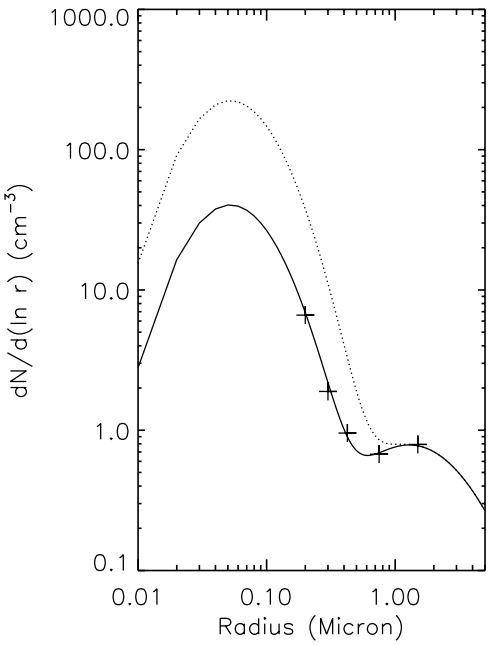

Figure 5. Observed (+) and fitted bimodal aerosol size distributions for baseline (solid) and polluted (dotted)

The size distribution N(r) for each mode of the lognormal aerosol distribution is given by

$$\frac{dN}{d\ln r} = \frac{N_t}{\sqrt{2\pi}\ln\sigma}\exp\left[-\frac{\ln^2(r/r_m)}{2\ln^2\sigma}\right] \quad (1)$$

where σ, r_m, and N_t are the standard deviation, geometric mean, and total number concentration, respectively. For mode 1 (smaller), these values are 2.04, 0.052 μm, and 72.2 cm^{-3}, respectively. For mode 2 (larger), these values are 2.5, 1.3 μm, and 1.8 cm^{-3}, respectively. While the lognormal size distributions provide a good fit to the measurements, there is some uncertainty in the fitted curves, especially at small aerosol sizes less than $\sim$0.1 μm in radius, where the HHPC-6 does not provide any information. The soluble portion of the aerosol is assumed to be ammonium bisulfate, based on evidence for the lack of full neutralization under remote Arctic conditions after transport over ocean [*Fridlind et al.*, 2000], with a soluble fraction of 0.9. Although an analysis of aerosol composition from MPACE is not available, we assume a high soluble fraction based on previous observations [*Zhou et al.*, 2001]. In the sensitivity tests designed to simulate polluted conditions (section 5), the N_t of the smaller mode is increased to 400 cm^{-3} (see Figure 5) which is typical of CN concentrations observed during springtime SHEBA in the presence of "Arctic haze" [*Yum and Hudson*, 2001]. Note that the geometric mean, standard deviation, and solubility of the aerosol may also impact the model, but for brevity we focus on the sensitivity to aerosol concentration.

[19] The number concentration of active ice nuclei is obtained from in situ out-of-cloud measurements on 9 and 10 October from the Continuous Flow Diffusion Chamber (CFDC) aboard the Citation aircraft [*Prenni et al.*, 2007]. These measurements represent the sum of ice nuclei less than 2 μm in aerodynamic diameter [*Rogers et al.*, 2001a] acting in deposition, condensation-freezing, and immersion-freezing modes. They indicate locally high concentrations of ice nuclei up to $\sim$10 L^{-1}, but a mean value of only 0.16 L^{-1}, which is near the detection limit of the instrument for the given flow rate. The removal of all particles >2 μm at the instrument's inlet represents a significant source of uncertainty, especially at warmer temperatures (see discussion by *Rogers et al.* [2001a]). In addition, the particles must nucleate and grow to 2 μm within the instrument residence time of $\sim$10 s. Thus these measurements may underestimate the number of IN if the nucleation mechanism is more probabilistic (and hence slower). A number of the samples ($\sim$90%) were below the detection threshold ($\sim$0.15 L^{-1}) of the sensor and were counted as 0 L^{-1}. Data are plotted as a function of processing temperature and ice supersaturation in Figure 6. These measured IN concentrations are very low relative to previous observations in the Arctic during springtime (SHEBA/FIRE-ACE) [*Rogers et al.*, 2001b], and in midlatitudes [e.g., *Meyers et al.*, 1992]. The average IN concentration for a given flight during SHEBA [*Rogers et al.*, 2001b] was one to two orders of magnitude larger than observed during MPACE. Thus sensitivity tests with increased IN concentration (section 5) assume 10 times and 100 times the mean value observed during M-PACE of 0.16 L^{-1}. The relatively low IN concentrations during MPACE are consistent with previous measurements in the Arctic during autumn (see discussion by *Prenni et al.* [2007]). Note that the number concentration of CN measured during SHEBA was about one order of magnitude larger than MPACE; using 100 times the IN concentration observed during M-PACE for the sensitivity test, combined with the baseline MPACE CN concentration of $\sim$70 cm^{-3}, produces an IN/CN ratio of about 200 ppm, which is near the upper limit of what was observed during SHEBA [*Rogers et al.*, 2001b]. While both the CCN and IN concentrations were larger during SHEBA than MPACE, we increase these concentrations separately in the sensitivity tests in order to separate the changes induced by either the CCN or IN. No direct measurements are available for the number of ice nuclei acting in contact-freezing mode although it is likely that their concentrations were also relatively low given the overall pristine conditions encountered during MPACE.

3. Model Description

[20] The polar MM5 is a nonhydrostatic model that includes parameterizations for: 1) shortwave and longwave radiative transfer, 2) boundary layer (BL) and turbulence processes, 3) surface processes and exchange with the overlying atmosphere, 4) cumulus convection, and 5) cloud microphysics. The nonhydrostatic momentum equations are solved using the time splitting method for sound wave stability described by *Grell et al.* [1994].

3.1. Model Configuration

[21] The shortwave and longwave radiative transfer follows *Briegleb* [1992a, 1992b]. Turbulent fluxes in the atmosphere and between the atmosphere and surface are parameterized following the 1.5-order prognostic turbulent kinetic energy (TKE) scheme described by *Janjic* [1994].

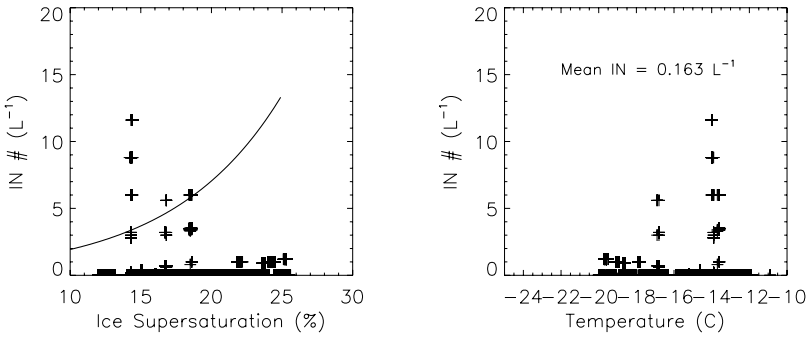

Figure 6. Out-of-cloud CFDC ice nuclei measurements from 9 and 10 October as a function of processing ice supersaturation and temperature. The formulation from *Meyers et al.* [1992], based on a collection of midlatitude measurements of condensation-freezing and deposition nuclei, is shown by the solid line.

Heat transfer through the land or sea ice-covered surface is predicted using a multilayer soil or sea ice and snow model depending upon the surface type [*Bromwich et al.*, 2001]. Turbulent transport is calculated for cloud droplets and ice, but neglected for precipitation species (rain and snow). The parameterization of deep convection is turned off since it did not occur during this period. The cloud fraction within a grid cell is unity if the water content predicted by the microphysics scheme is greater than 10^{-5} g m^{-3} at any level, and zero otherwise.

[22] MM5 offers the flexibility of grid nesting. We utilize two domains centered on North Slope of Alaska and adjacent Arctic Ocean (Figure 7). This configuration allows us to capture the three important surface types across the region: pack ice in the central Arctic Ocean, open ocean of the Beaufort Sea, and snow covered land over northern Alaska. The outer and inner domains have grid spacings of 30 and 10 km, respectively. Results from the inner domain are presented here. Simulations are performed with 34 vertical levels and 15 levels in the lowest 1 km. These horizontal and vertical grid spacings are chosen since they are typical for high-resolution numerical weather prediction and regional climate models. At such resolution, the model is obviously not able to resolve cloud-scale features, such as the individual roll and cellular structures seen in Figure 3. Thus sensitivities that result from small-scale features (e.g., entrainment) will not be captured. However, this resolution allows us to use a domain that is large enough to capture key regional variability (especially in surface type), focusing in particular on differences in model sensitivity between the open ocean region of the Beaufort Sea and snow covered land of northern Alaska. This configuration also allows us simulate key synoptic-scale features, namely, the cold airflow from the pack ice, across the open ocean, and into northern Alaska.

[23] The initial and lateral boundary conditions are specified using NCEP Eta analyses, except for the lateral boundary conditions at 0600 UTC which are given by the Eta forecast from the run starting 0000 UTC. The period simulated is from 0000 UTC 9 October to 1200 UTC 10 October. A potential weakness in comparing model results with observations is that the model represents a grid-average value over 10 km, while the observations are single-point measurements. For the aircraft data, measurements are limited in both space and time. To minimize these concerns, the quantitative comparison focuses mainly on time-averaged data. Time-averaged data over the period 1200 UTC 9 October to 1200 UTC 10 October are analyzed, which allows for 12 h of model spin-up time.

3.2. Description of the Cloud Microphysics

[24] The two-moment microphysics scheme is described in detail by *Morrison et al.* [2005a] and MP05. Prognostic variables include the mixing ratios and number concentrations of cloud (small) ice, cloud droplets, snow, and rain. The hydrometeor size distributions are modeled using generalized gamma functions, with several parameterized microphysical processes acting to transfer mass and number between the various species. A detailed treatment of droplet activation and ice nucleation from a distribution of CCN and IN is included, allowing us to simulate the impact of aerosols on both liquid and ice microphysics in mixed-phase clouds. These parameterizations are described in more detail below.

[25] Two different modes of heterogeneous ice nucleation are considered by the model. Since the CFDC is not able to distinguish between deposition, condensation-freezing, and immersion-freezing, these three mechanisms are considered as a single mode (hereafter referred to as 'DCI') in the model, with the number concentration of ice nuclei acting in this mode given by the mean CFDC concentration of 0.16 L^{-1}. Given the lack of correlation (see Figure 6), no

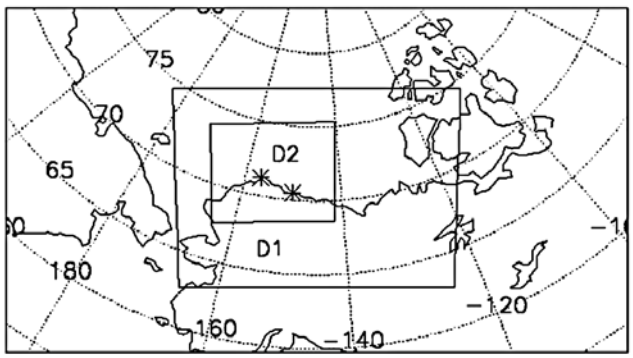

Figure 7. Location of the two MM5 domains (D1 and D2). Barrow and Oliktok point are indicated by *.

variation of IN concentration with ice supersaturation or temperature is considered. Depletion of ice nuclei is not considered here due to the difficulty of specifying sources over different surfaces including the open ocean, which may potentially serve as an important source for biogenic ice nuclei [e.g., *Schnell*, 1977]. The other heterogeneous mode included in the model is contact freezing. The CFDC did not directly measure ice nuclei active in contact mode. Given the lack of observations, we assume that the number concentration of contact nuclei is a function of temperature following *Meyers et al.* [1992]. This parameterization is an empirical fit to midlatitude measurements. For the conditions found here, $2-3\ L^{-1}$ of contact IN are available near cloud top; however, the actual number of crystals produced by contact nucleation is far lower since collisions between the contact nuclei and water droplets are required to form ice particles by this mechanism. Given the observed low concentrations of IN measured by the CFDC, it is likely that the number of contact IN is also low relative to midlatitude observations. However, our results here exhibit little sensitivity to contact nucleation. This finding differs from our previous SHEBA modeling study [*Morrison et al.*, 2005c], which likely reflects the warmer cloud temperatures and neglect of IN depletion here. We therefore focus on sensitivity to the "DCI" nucleation mechanisms in this study.

[26] The CCN spectrum as a function of the aerosol chemical and physical properties is given by the parameterization of *Abdul-Razzak and Ghan* [2000]. Relevant parameters are N_t, r_m, σ, soluble fraction, and chemical composition of the soluble part of the aerosol. The number of droplets activated is also a function of environmental conditions (temperature, pressure) and vertical velocity [see *Abdul-Razzak and Ghan*, 2000]. Since local rather than grid-scale vertical velocity is needed for droplet activation, a parameterization for the standard deviation of the sub-grid vertical velocity was developed by MP05. This characteristic sub-grid vertical velocity w' is related to the predicted TKE assuming that $w' = u' = v'$ (where u' and v' are the turbulent horizontal velocity components):

$$w' = \left(\frac{2}{3} TKE\right)^{\frac{1}{2}} \tag{2}$$

In this study, aerosol properties (along with ice nuclei) are specified as described in section 2.3, and assumed to be constant in height and time throughout the model domain.

[27] Additional upgrades have been made to the microphysics scheme relative to MP05 and MP06. A new parameterization has been implemented that captures changes in the riming rate as a function of droplet size since a goal of this study is to investigate the impact of droplet size on ice microphysics and snowfall. The collection efficiency for riming of cloud ice/snow by droplets is a function of the Stokes number following *Thompson et al.* [2004], rather than unity as assumed by MP05 and MP06 (note that here the riming collection efficiency is still unity for rain-snow collisions). The collection of droplets by cloud ice (neglected by MP05 and MP06) is allowed when the mean cloud ice diameter exceeds 100 μm. This assumed size threshold is based on observed and theoretical values [see *Pruppacher and Klett*, 1997, and references therein] that vary between about 100–300 μm for planar and platelike crystals, and about 35–50 μm in terms of width for columnar crystals. Note that in the present scheme, the crystal shape is not explicitly specified; instead, spherical crystals are assumed with bulk density following *Morrison et al.* [2005a] for microphysical process calculations. For sedimentation, the terminal fallspeed-size relationship for snow is from *Locatelli and Hobbs* [1974] assuming 'aggregates of unrimed assemblages of plates, side planes, bullets, and columns', and for cloud ice from *Ikawa and Saito* [1990].

[28] In most models, ice multiplication (i.e., processes that result in secondary ice initiation and a crystal concentration greater than the ice nucleus concentration) is parameterized following the rime splintering mechanism described by *Hallett and Mossop* [1974]. Given that rime splintering is believed to be limited to temperatures between -3 and -8°C [*Hallett and Mossop*, 1974], it likely did not occur in the real cloud layer given that the temperature was colder than this range (at least in the vicinity of the coastline between Barrow and Oliktok Point where the measurements were obtained). Thus rime splintering has been neglected in the simulations shown here. Note that when rime splintering is included in the model, it produces a significantly enhanced crystal concentration (by a factor of 3–4), and somewhat increased ice water content and surface precipitation rate, but has little impact on the liquid water characteristics, relative to the baseline results shown in the next section. Rime splintering occurs in this instance because of a bias in the simulated cloud height and hence temperature by 2–3 K that is described in more detail in the next section. Despite its impact on the simulated ice characteristics, whether or not rime splintering is included in the model has little impact on the overall results of the sensitivity analysis described in section 5.

[29] In MP05 and MP06, the shortwave cloud radiative properties were given by *Slingo* [1989] for droplets and *Ebert and Curry* [1992] for ice as a function of effective radius and liquid or ice water content, as implemented in the NCAR Community Climate Model Version 2 (CCM2). Aerosols have no direct impact on the radiative transfer in the model, allowing us to focus on indirect rather than direct aerosol radiative effects. In order to simulate the impact of droplet size on cloud emissitivity, additional changes have been made to the longwave cloud-radiative properties relative to the CCM2 radiation package. Here, the broadband mass absorption coefficient k_c ($m^2\ g^{-1}$) is a function of droplet effective radius, r_e, following *Savijarvi and Raisanen* [1998]:

$$k_c = 0.31 \exp(-0.08 r_e). \tag{3}$$

4. Baseline Results

[30] The baseline simulation with configuration as described above produces a widespread low-level cloud layer over the open ocean and extending into the North Slope of Alaska consistent with the observations. The cloud layer is mixed-phase with ice precipitation reaching the surface. Most of the layer is dominated by the liquid phase except near cloud base (Figure 8). To the northeast of Oliktok Point

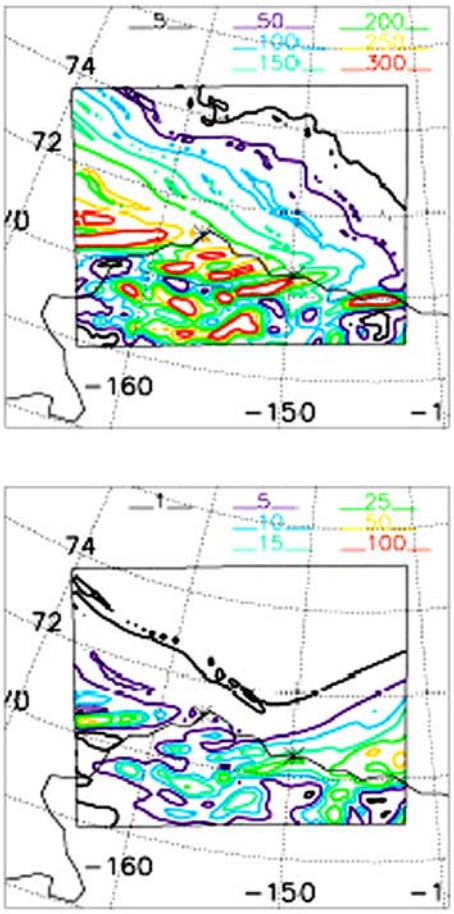

Figure 8. Baseline modeled liquid water path (g m^{-2}) (top) and ice water path (g m^{-2}) (bottom) at 1200 UTC October 10. Barrow and Oliktok Point are indicated by *.

over the Beaufort Sea is a region of fairly large IWP (>25 g m^{-2}) associated with upper-level ice clouds in the simulation. The distinct bands of higher LWP located along the coast and inland over the North Slope are associated with diabatically driven mesoscale circulations (with maximum vertical velocity ~5 cm/s and horizontal scale of about 30–100 km). These circulations are distinct from the smaller-scale cloud rolls and streaks seen in Figure 3 that the model cannot resolve. The simulated precipitation rate lies within the large spread between the NWS and ARM observations at Barrow. The sea level pressure, surface air temperature and near-surface winds produced by MM5 at 1200 UTC 10 October 10 (Figure 9) are generally similar to the corresponding Eta analysis (see Figure 2). However, the simulated near surface air temperatures along the Brooks Range are warmer by 5–10 K.

[31] The modeled LWP is quite similar to retrievals at Barrow, but larger than retrieved at Oliktok Point, especially after 1200 UTC on 10 October (Figure 10). The mean LWP derived from in situ aircraft observations on 9 and 10 October is about 130–160 g m^{-2}, which lies between the retrieved values at Barrow and Oliktok Point. An obvious difference between the modeled and retrieved time series of LWP is the much larger variability in the retrievals. The higher frequency variability over timescales less than 1 hr reflects retrieval noise and cloud-scale structures that cannot be resolved by the model.

[32] The model captures general features of the aircraft microphysical observations, especially for the liquid hydrometeors (Figure 11). For ice, the modeled values are calculated by neglecting particles smaller than 53 μm for consistency with the observations (see section 2.1). The neglect of these particles results in a reduction of the crystal concentration of generally less than 10%, and has little impact on IWC. The modeled microphysical quantities are averaged over the period 1200 UTC 9 October to 1200 UTC 10 October at Barrow and Oliktok Point and compared with average measurements from the two flights that took place between 2000 UTC 9 October and 0300 UTC 10 October. Both the modeled and observed profiles of liquid water content and effective radius increase with height, although the modeled values tend to be somewhat larger for both quantities. Variability in the observed liquid water content is largest near the cloud top, which probably reflects the impact of entrainment. The modeled and observed droplet number concentrations are fairly constant with height for a given profile. However, there is some variability in the observed droplet concentrations between the profiles (ranging from about 30 to over 100 cm^{-3}), suggesting local variability of the aerosol.

[33] The model is not able to capture the ice microphysics as well as the liquid quantities. However, the observed ice water content and number concentration vary substantially over space and time and are associated with a larger degree of uncertainty than the liquid microphysical quantities [*McFarquhar et al.*, 2007]. The modeled crystal concentration is smaller than observed by about one order of magnitude; the impact of increasing the IN number concentration (and hence crystal concentration) in the model is described in the next section. The under-prediction of crystal concentration relative to the aircraft observations is

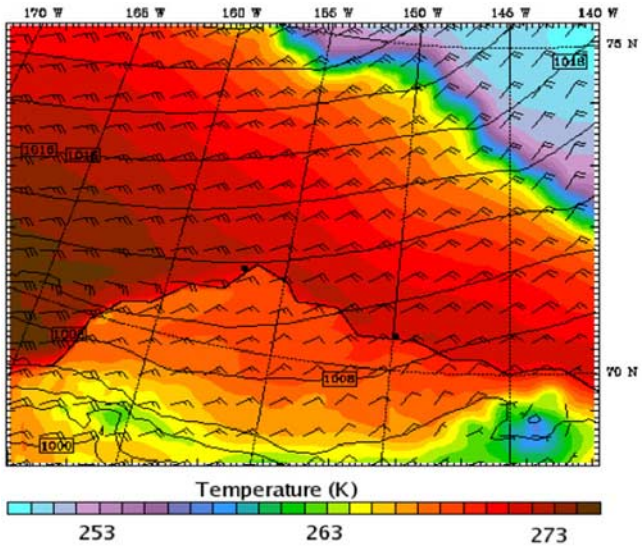

Figure 9. Surface air temperature (color contours), sea level pressure (black contours, interval of 2 mb), and near surface winds (barbed vectors, full barb = 5 m s^{-1}) simulated by MM5 for 1200 UTC 10 October. Barrow and Oliktok Point are indicated with black dots.

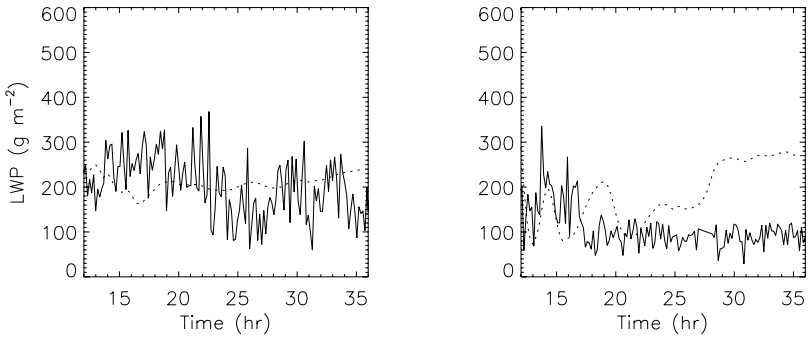

Figure 10. Time series of retrieved (solid) and modeled (dotted) liquid water path for Barrow (left) and Oliktok Point (right). Instantaneous modeled and retrieved data is plotted every 10 minutes over the period from 1200 UTC 9 October to 1200 UTC 10 October.

a consequence of the large discrepancy between the observed IN and ice crystal concentrations. As suggested by *Fridlind et al.* [2007], this discrepancy implies that additional ice initiation mechanisms (i.e., mechanisms not included in most current microphysics schemes, including ours) may have acted to enhance the concentration of ice crystals in the real cloud layer. *Fridlind et al.* [2007] suggest that two mechanisms may be strong enough to account for the discrepancy: formation of ice nuclei from drop evaporation residuals, and drop freezing during evaporation; they

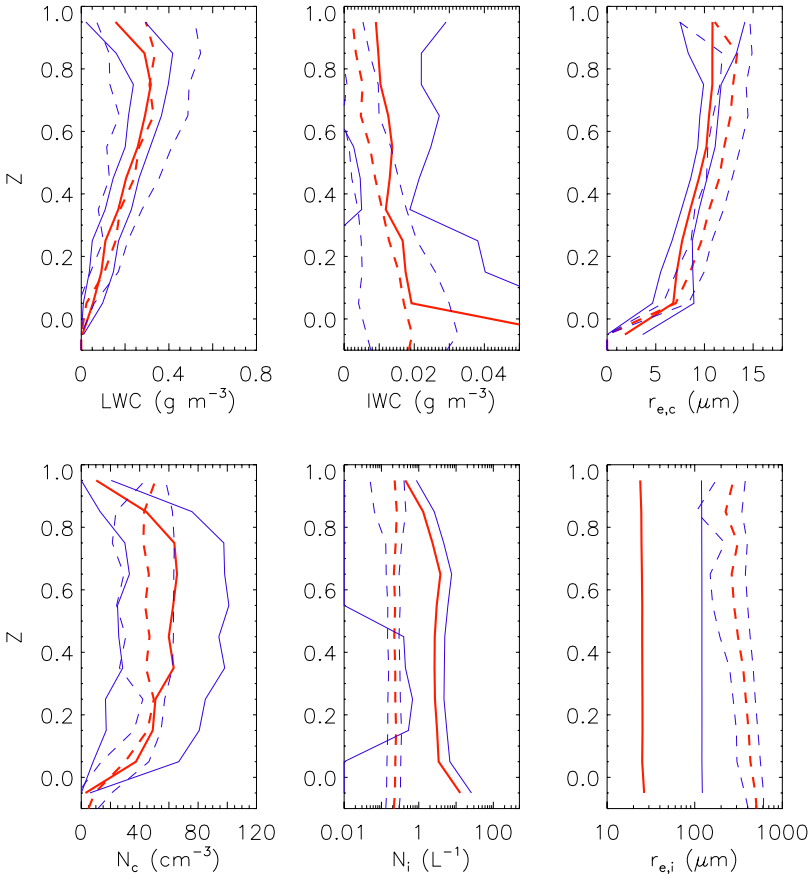

Figure 11. Comparison of modeled (dash red) and aircraft observed (solid red) liquid water content (*LWC*), ice water content (*IWC*), droplet effective radius ($r_{e,c}$), droplet number concentration (N_c), ice crystal concentration (N_i), and ice effective radius ($r_{e,i}$) as a function of normalized height (Z) with respect to the cloud layer (0 = cloud bottom, 1 = cloud top). The modeled profiles are averages over the period 1200 UTC 9 October –1200 UTC 10 October for the Barrow and Oliktok Point grid cells. The aircraft profiles are averaged over the two flights that took place between 2000 UTC 9 October and 0300 UTC 10 October. The blue dash and solid lines indicate the mean ± one standard deviation for the model and aircraft data, respectively.

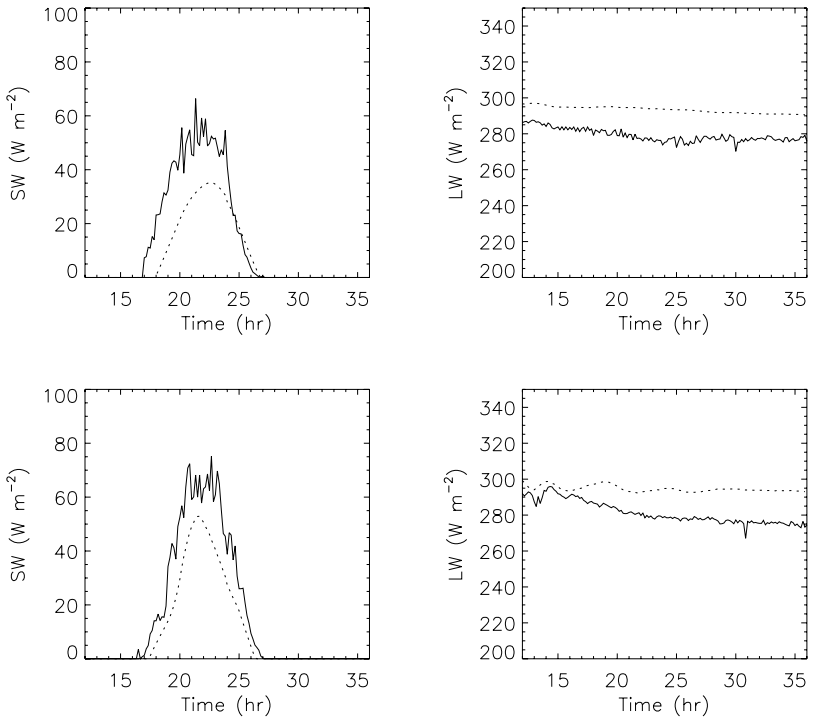

Figure 12. Time series of observed (solid) and modeled (dotted) downwelling shortwave (SW) and longwave (LW) radiative fluxes at the surface for Barrow (top) and Oliktok Point (bottom). Instantaneous modeled and retrieved data is plotted every 10 m over the period from 1200 UTC 9 October to 1200 UTC 10 October.

note that additional "process-oriented" measurements are needed to distinguish among possible mechanisms in future field experiments.

[34] The modeled ice effective radius (calculated by mass-weighting the values for cloud ice and snow) is significantly larger than observations, which is consistent with the under-prediction of crystal concentration. Differences in the assumed mass-dimension (*m-D*) relationship also lead to the differences in effective radius; both the in situ observations and the model assume $m = aD^b$, but $b = 1.7$ for the observations, and $b = 3$ for the model. Differences in ice effective radius have little impact on the radiative fluxes since the cloud is dominated by liquid.

[35] Although the model is able to reasonably capture the profiles of the liquid cloud microphysical quantities on normalized height coordinates, the model consistently underestimates both the cloud top and base heights by about 200–500 m at Barrow (not shown). The model produces similar cloud height at both Barrow and Oliktok Point. Thus the bias at Oliktok Point is not as severe, owing to the lower observed cloud boundaries, but the cloud base and top are still underestimated in the simulation by 100–300 m. The exact cause of this bias is not known, but may reflect uncertainties in the boundary layer parameterization. The major consequence of the bias in cloud boundaries is the overestimation of cloud base temperature by ~2–3 K, which results in a bias in the downwelling longwave radiative flux as described below. It also results in spurious ice multiplication via rime splintering when this mechanism is allowed, as described in the previous section.

[36] Despite reasonable similarity between the simulated and observed liquid cloud microphysical quantities which dominate the cloud radiative properties, the simulated downwelling solar and longwave fluxes at the surface show notable differences relative to the observations (Figure 12, see also Table 2). The downwelling solar flux at the surface during this period is much smaller than the longwave flux due to extended periods of darkness and large solar zenith angles; the daily mean downwelling solar flux is about an order of magnitude smaller than the downwelling longwave flux (Table 2). The modeled downwelling longwave flux is persistently too large by 5–20 W m^{-2}. This bias is attributed primarily to the bias in cloud height and hence emission temperature (2–3 K warmer than observed); at Barrow and Oliktok Point the modeled and observed clouds have large enough water paths that they both emit nearly as blackbodies. Differences between the modeled and observed downwelling solar fluxes are mostly attributed to uncertainty in the surface albedo that was specified from the Eta analyses (surface albedo impacts the downwelling flux due to multiple reflections between the cloud and surface), as well as difficulty in treating the radiative transfer at large solar zenith angles.

5. Sensitivity Tests and Discussion

[37] A number of sensitivity experiments examine the impact of CCN and IN number concentrations on the simulated cloud microphysics, surface radiative fluxes, and dynamics. The various experiments are listed in Table 1. The first group of sensitivity tests (POLL,

Table 1. List of the MM5 Runs

Run	Description
BASE	Baseline
POLL	small mode aerosol concentration increased to 400 cm^{-3} (polluted)
BASE-CEFF	collection efficiency for riming of cloud droplets and rain by cloud ice and snow set to 1
POLL-CEFF	collection efficiency for riming of cloud droplets and rain by cloud ice and snow set to 1; small mode aerosol concentration increased to 400 cm^{-3} (polluted)
IN × 10	number concentration of DCI ice nuclei increased by a factor of 10
IN × 100	number concentration of DCI ice nuclei increased by a factor of 100

BASE-CEFF, POLL-CEFF) examine the impact of increased CCN concentration associated with polluted aerosol conditions, including the impact on droplet riming collection efficiency. The second group of sensitivity runs (IN × 10 and IN × 100) examines the impact of increased IN concentration. Time-averaged results from 1200 UTC 9 October to 1200 UTC 10 October for the Barrow grid are shown in Table 2; similar results are produced for the Oliktok Point grid (not shown).

[38] To test the impact of increased CCN number concentration, the aerosol concentration of the smaller mode is increased to 400 cm^{-3} for the polluted aerosol runs, mimicking typical 'Arctic haze' conditions as measured during springtime SHEBA [*Yum and Hudson*, 2001] (see Figure 5). As expected, the polluted aerosol run (POLL) exhibits a much larger mean value of N_c and smaller mean value of r_e (by about 4 μm) compared to the baseline run (BASE). The increased aerosol loading also results in greater LWP and reduced IWP and precipitation rate at the surface at Barrow (note that 60–70% of the total precipitation consists of snow in all of the runs). A more significant increase in LWP (>75 g m^{-2}) in POLL relative to BASE occurs to the west and south of Barrow (Figure 13). Cloud fraction does not differ significantly between these runs.

[39] Additional sensitivity experiments (BASE-CEFF and POLL-CEFF in Table 1) help to discern the impact of changes in riming collection efficiency as the aerosol loading is increased. In these tests, riming collection efficiency for cloud droplets is unity for both baseline (BASE-CEFF) and polluted (POLL-CEFF) aerosol conditions, in contrast to the size-dependent riming collection efficiency used in BASE and POLL. The modeled cloud parameters are more sensitive to changes in CCN concentration when riming collection efficiency is allowed to vary (as in BASE and POLL). Calculating the relative differences in LWP, IWP, and precipitation rate between BASE-CEFF and POLL-CEFF for the Barrow grid cell (+13.2, −36.4, −33.3%, respectively), and comparing with the corresponding differences in LWP, IWP, and precipitation rate between BASE and POLL (+15.8, −48.3.4, −61.5%, respectively), suggests that the change in droplet collection efficiency due to polluted conditions accounts for about one-fourth to one-half of the difference in IWP and precipitation rate and about one-fifth of the difference in LWP between BASE and POLL. The remaining differences in IWP, precipitation rate, and LWP are mostly attributed to decreased droplet collision-coalescence and supercooled drizzle formation as the aerosol loading is increased.

[40] The impact of increased CCN under polluted conditions is also examined in terms of the indirect impact on the surface radiative fluxes through modification of the clouds. The increase in LWP and decrease in r_e with increased aerosol loading in POLL produces a small decrease (2.9 W m^{-2}) in the mean downwelling solar flux compared to BASE (see Table 2). The impact at solar noon is more significant (decrease of 13.5 W m^{-2}). However, there is almost no impact on the downwelling longwave flux since the clouds in the Barrow grid cell emit nearly as blackbodies in both BASE and POLL. In the northeast section of the domain near the pack ice edge the clouds contain less water and cloud emissivity is susceptible to changes in r_e. The longwave indirect effect in this region increases the downwelling longwave flux at the surface by up to ~10 W m^{-2} in POLL relative to BASE (Figure 14). Similarly, thinner clouds in the southwest and southeast

Table 2. Modeled and Observed Time-Averaged Liquid Water Path (*LWP*), Ice Water Path (*IWP*), Droplet Number Concentration (N_c), Droplet Effective Radius ($r_{e,c}$), Total (Cloud Ice Plus Snow) Number Concentration (N_i), Ice Effective Radius ($r_{e,i}$), Downwelling Surface Longwave Radiative Flux (*LW*), Downwelling Surface Solar Flux (*SW*), and Liquid-Equivalent Precipitation Rate (*PREC*) for the Barrow Grid Cell[a]

Run	*LWP* G m^{-2}	*IWP* g m^{-2}	N_c cm^{-3}	$r_{e,c}$ μm	N_i L^{-1}	$r_{e,i}$ μm	*LW* W m^{-2}	*SW* W m^{-2}	*PREC* mm/h
Observed	223.3	-	-	-	-	-	279.1	13.3	~0.01–0.1
BASE	208.7	2.9	50.6	11.1	0.16	273.0	293.4	7.8	0.026
POLL	241.7	1.5	234.4	7.1	0.21	203.2	293.5	4.9	0.010
BASE-CEFF	204.7	3.3	50.4	11.1	0.16	284.0	293.3	7.8	0.033
POLL-CEFF	231.7	2.1	235.6	7.1	0.20	237.3	293.3	5.0	0.022
IN × 10	157.7	9.3	48.9	11.0	1.56	178.2	292.7	9.6	0.058
IN × 100	30.3	34.9	44.4	8.8	11.30	116.6	290.8	17.5	0.085

[a]The various model runs are defined in Table 1. Time averaging is between 1200 UTC 9 October and 1200 UTC 10 October.

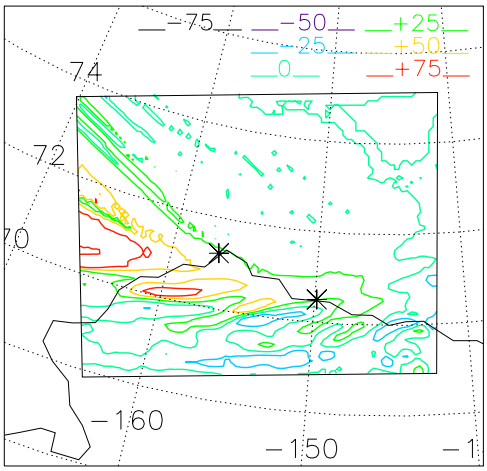

Figure 13. Difference in time-averaged liquid water path between POLL and BASE (g m^{-2}). Time averaging is between 1200 UTC 9 October and 1200 UTC 10 October.

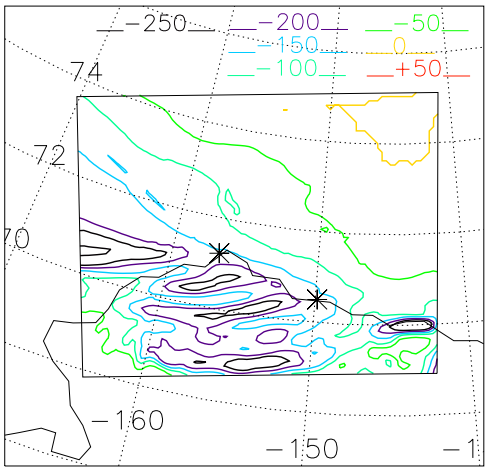

Figure 15. Difference in time-averaged liquid water path between IN × 100 and BASE (g m^{-2}). Time averaging is between 1200 UTC 9 October and 1200 UTC 10 October.

corners of the domain are also susceptible to changes in emissivity and are therefore associated with an increase in the downwelling longwave flux that exceeds 10 W m^{-2}.

[41] The sensitivity to increased ice nucleus concentrations (deposition, condensation-freezing, and immersion modes only) is examined in runs IN × 10 and IN × 100, with the baseline concentration of 0.16 L^{-1} increased by factors of 10 and 100, respectively, giving concentrations of 1.6 and 16 L^{-1}. These higher ice nucleus concentrations are similar to mean IN measurements during springtime SHEBA of about one to a few tens per liter [*Rogers et al.*, 2001b]. In general, the simulated stratocumulus layer is more sensitive to IN concentration than CCN concentration, for the range of values tested here. Increasing the IN concentration reduces the LWP and increases IWP and precipitation in the Barrow grid cell (see Table 2) consistent with previous studies [e.g., *Harrington et al.*, 1999; *Jiang et al.*, 2000; *Prenni et al.*, 2007]. This occurs mostly because of the increased strength of the Bergeron-Findeisen process (i.e., transfer of water from droplets to ice due to the lower saturation vapor pressure with respect to ice). The decrease in LWP occurs throughout the mixed-phase stratocumulus region (Figure 15), but is most pronounced over the North Slope where the surface turbulent water vapor fluxes are small. The mesoscale circulations over the North Slope evident in BASE are much weaker with the substantial reduction of LWP in IN × 100. Note that the average ice crystal concentration of about 1.6 L^{-1} from IN × 10 is much closer to the aircraft observations than BASE (see Figure 11), while IN × 10 is still able to reproduce reasonably the liquid microphysical characteristics (although the mean LWP is somewhat smaller than observed at Barrow, see Table 2).

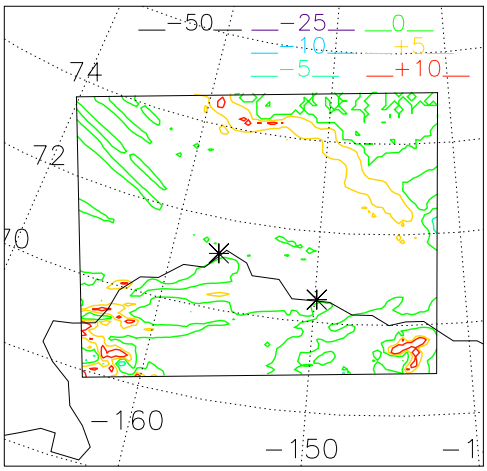

Figure 14. Difference in time-averaged downwelling longwave radiative flux at the surface (W m^{-2}) between POLL and BASE. Time averaging is between 1200 UTC 9 October and 1200 UTC 10 October.

[42] *Prenni et al.* [2007] examined the same MPACE case study using the Regional Atmospheric Modeling System (RAMS). Although RAMS exhibited similar sensitivity with respect to increasing the IN concentration (i.e., significant decrease in LWP and increase in IWP), in contrast to our results, Prenni et al. found that depletion of IN was required to maintain liquid water, even with the low concentrations of IN observed during MPACE. Without a rigorous model intercomparison, it is not possible to determine the exact factors leading to the differences between our results and those of Prenni et al., although this analysis suggests that our model has less ice growth at the expense of liquid water relative to RAMS (perhaps due to a weaker Bergeron process), at least for this particular case.

[43] The impact of increased IN concentration on the surface radiative fluxes is also examined. The downwelling longwave flux at the surface is decreased throughout the mixed-phase region in IN × 10 and especially IN × 100 (although the longwave flux is increased for the upper-level ice cloud region northeast of Oliktok Point). However, this decrease is most pronounced in two regions (Figure 16): 1) near the pack ice edge where LWP is fairly small, and hence where the cloud emissivity is susceptible to a reduction in LWP, and 2) over the North Slope of Alaska where LWP is reduced substantially compared to BASE, leading to lower cloud emissivity. Over the open ocean between these two regions, the clouds still act as near blackbodies even with

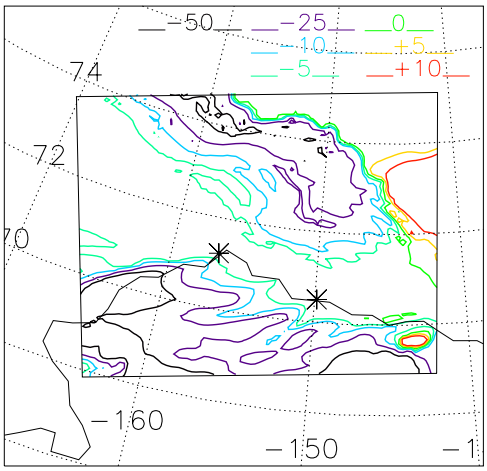

Figure 16. Difference in time-averaged downwelling longwave radiative flux at the surface (W m^{-2}) between IN × 100 and BASE. Time averaging is between 1200 UTC 9 October and 1200 UTC 10 October.

the reduction in LWP, so that there is much less impact on the surface downwelling longwave fluxes. In this region (and in the Barrow grid cell; see Table 2), the increase in mean downwelling solar flux at the surface is larger in magnitude than the decrease in the mean downwelling longwave flux. However, farther inland over the North Slope the decrease in downwelling longwave flux dominates and strongly impacts the surface energy budget. By the end of the simulation (1200 UTC 10 October), surface temperatures in this region are 3–6 K colder in IN × 100 compared to BASE.

[44] Despite fairly significant differences in the LWP and cloud radiative forcing between IN × 100 and BASE, the large-scale dynamics are quite similar (this similarity is noted among all of the sensitivity runs). In contrast, the large-scale dynamics were more sensitive to the microphysics for the SHEBA case simulated by MP06; namely, there was a decrease in the anticyclogenesis and surface pressure across the domain with reduction of LWP. This difference between our results and MP06 may be due to differences in the horizontal scale of the cloud-induced changes of surface and lower-tropospheric temperatures. Here, changes in temperature due to reduction of LWP in IN × 100 occur over a fairly limited area of the domain (over interior North Slope of Alaska), in contrast to the widespread changes in MP06.

[45] There is uncertainty in other microphysical parameters in the model, especially for the ice phase. While model results may be expected to exhibit some sensitivity to these parameters, the relevant question here is whether uncertainties in these parameters impact the model sensitivity to CCN and IN. As an example, we have run additional simulations (both with baseline and elevated IN and CCN concentrations) with the size threshold for autoconversion of cloud ice to snow, D_{cs}, varied between 100 and 500 μm (the baseline value is 250 μm). This size threshold represents a key parameter in the bulk microphysics scheme that is not well constrained by bin models or observations. While the important cloud parameters (mean LWP and IWP) vary by up to ~20% for given IN and CCN concentrations with modification of D_{cs}, the sensitivity to IN and CCN concentrations is similar among the runs. These results suggest robustness of our results in terms of these sensitivities, at least with regard to uncertainties in D_{cs}; it is beyond the scope of this paper to perform a similar analysis for every parameter in the model.

6. Summary and Conclusions

[46] In this study we used a modified version of the MP05 two-moment bulk microphysics scheme implemented into the Polar-MM5 to simulate low-level mixed-phase clouds observed during MPACE. Modifications to the microphysics scheme included the addition of a droplet size-dependent riming collection efficiency and droplet size-dependent longwave mass absorption coefficient. These changes allowed us to examine the impact of droplet size on ice microphysics and precipitation as well as cloud emissivity. Results were compared with in situ microphysical and radiative measurements and remotely based retrievals of LWP. Several sensitivity simulations were also performed to assess the sensitivity of the modeled cloud properties and surface radiative fluxes to changes in the CCN and IN number concentrations.

[47] The following is a summary of the main findings:

[48] 1) The model was able to reproduce reasonably the observed liquid microphysical cloud characteristics. However, the model produced less ice than was observed, especially in terms of the number concentration. This under-prediction was associated with a large discrepancy between the observed ice nucleus and ice crystal concentrations, suggesting that additional ice initiation mechanisms not included in our model (or other current models) may have occurred in the real cloud layer, assuming no large, undiagnosed errors in the measurements. A detailed discussion of some of these potential ice initiation mechanisms is given by *Fridlind et al.* [2007]. Note that rime splintering [*Hallett and Mossop*, 1974], which is typically the only ice multiplication process included in models, cannot explain the discrepancy because the real cloud layer in this study was colder than the temperature range over which rime splintering is believed to operate.

[49] 2) Despite the reasonably accurate simulation of the liquid microphysics (which dominated the cloud radiative properties), the downwelling shortwave and longwave radiative fluxes at the surface were somewhat biased. The modeled downwelling longwave flux was persistently too large by 5–20 W m^{-2} due to a bias in the cloud height and hence emission temperature.

[50] 3) Increasing the CCN concentration produced smaller droplets, increased LWP, and decreased IWP and snowfall rate in the model. Two processes contributed to these changes: 1) decreased riming efficiency of cloud ice and snow by droplets and 2) decreased droplet collision-coalescence and hence production of supercooled drizzle.

[51] 4) Increasing the CCN concentration had little impact on the longwave fluxes at the surface despite a significant decrease in droplet effective radius. This was because both the polluted and pristine clouds emitted nearly as blackbodies; an exception was the marginal zone near the sea ice edge where the LWP was low and hence cloud emissivity responded to changes in droplet size. The overall

insensitivity of the longwave fluxes to droplet size, in contrast to the studies of *Garrett et al.* [2002], *Garrett and Zhou* [2006], and *Lubin and Vogelmann* [2006], reflects the fairly unique nature of the MPACE stratocumulus, with much higher amounts of condensed water than most low-level arctic stratiform clouds. Increased aerosol loading also led to a decrease in the downwelling solar flux at the surface of a few W m^{-2}, which had little impact on the total radiative flux at the surface due to the dominance of the longwave flux (owing to the large solar zenith angle during this period).

[52] 5) Increasing the IN concentration to values more typical of measurements from the springtime Arctic reduced the LWP and increased the IWP and precipitation rate. The impact on LWP and cloud emissivity was most significant inland over the North Slope of Alaska, leading to reduced surface temperatures. The impact on LWP, cloud emissivity, and lower-tropospheric temperature over the open ocean was much smaller due to the large forcing provided by the surface turbulent heat and moisture fluxes. Contact nucleation had less impact than in our previous SHEBA studies [e.g., *Morrison et al.*, 2005c], which may have been due to our neglect of IN scavenging and the warmer cloud temperatures for MPACE. Inclusion of IN scavenging here most likely would have resulted in even smaller crystal concentrations compared with observations, which were already lower than observed. *Prenni et al.* [2007] found that scavenging of IN was needed to maintain liquid water in their model even with the low IN concentrations observed during MPACE observations, in contrast to our results.

[53] 6) Reduction of LWP due to increased IN concentration reduced the strength of mesoscale circulations over the North Slope of Alaska, but there was almost no impact on the large-scale dynamics. This likely reflected the limited and discontinuous horizontal extent of changes in lower-tropospheric air temperature as the LWP was reduced, in contrast to the widespread changes in the SHEBA modeling study of MP06.

[54] Overall, the sensitivity of the modeled mixed-phase clouds to CCN and especially IN concentrations was dependent on the underlying surface conditions. During this period, most of the domain was covered with open water which provided a significant source of heat and moisture. Thus over the open ocean the condensed water mass remained large despite changes in the concentrations of CCN and IN, and the clouds continued to emit as blackbodies except near the pack ice edge. In contrast, the LWP and hence cloud emissivity was quite sensitive to the IN concentration over snow covered land. This sensitivity over land was consistent with previous modeling studies of mixed-phase stratus over sea ice [e.g., *Pinto*, 1998; *Harrington et al.*, 1999; *Jiang et al.*, 2000], where surface turbulent fluxes also tend to be much smaller than over the open ocean here.

[55] Despite uncertainties in the representation of ice initiation in current models, it is important to understand the behavior of these models in terms of their sensitivity to ice nuclei, especially since more climate and weather prediction models are beginning to utilize schemes that explicitly predict ice crystal concentration from a specified or predicted population of ice nuclei [e.g., *Lohmann*, 2002; *Thompson et al.*, 2004; *Liu et al.*, 2007]. The discrepancy between the observed IN and ice crystal concentrations, leading to the significant underprediction of crystal concentration reported here, is suggestive of missing ice initiation processes in current models [see discussion in *Fridlind et al.*, 2007], including ours. An important area of future research will be to determine how the sensitivity to ice nuclei exhibited by current models is altered as the treatment of ice initiation is improved.

[56] Since the model was not able to resolve finer-scale features of the stratocumulus layer using a horizontal grid spacing of 10 km, we could not address the impact of accompanying changes in the cloud-scale dynamics and entrainment rate as the CCN and IN concentrations were modified. The large-eddy modeling study of *Ackermann et al.* [2004] suggested that under certain conditions, an increase in the CCN concentration can lead to a decrease in the LWP in subtropical stratocumulus (in contrast to our results here) due to increased entrainment of dry air into the BL. Of course, arctic mixed-phase stratocumulus differ from subtropical stratocumulus, most notably by the presence of ice and the frequent presence of water vapor mixing ratio inversions at the top of the BL [*Curry et al.*, 1996]. High-resolution cloud models applied to MPACE stratocumulus with appropriate microphysical packages should help to address interactions between the microphysics and cloud-scale dynamics.

[57] **Acknowledgments.** This work was funded by DOE ARM DE-FG02-03ER63539 and NASA MAP NNG06GBB1G. Contributions of H. Morrison were also funded by the National Center for Atmospheric Research Advanced Study Program. The National Center for Atmospheric Research is sponsored by the National Science Foundation. Contributions of G. McFarquhar were funded by DOE ARM Contract DE-FG03-02ER63337 and by the ARM Uninhabited Aerospace Vehicle (UAV) Program. Data were obtained from the ARM program archive, sponsored by DOE, Office of Science, Office of Biological and Environmental Research, Environmental Sciences Division. We thank C. Long for providing the ARM surface radiative fluxes, A. Prenni for providing the CFDC ice nuclei measurements, J. Verlinde for providing the map of the MPACE domain, D. Turner for providing the liquid water path retrievals, and J. Y. Harrington for helpful discussion. Comments on the manuscript by P. Field and G. Thompson are appreciated. We also thank three anonymous reviewers whose comments greatly improved the quality of the paper.

References

Abdul-Razzak, H., and S. J. Ghan (2000), A parameterization of aerosol activation 2. Multiple aerosol types, *J. Geophys. Res.*, *105*(D5), 6837–6844.

Ackermann, A. S., M. P. Kirkpatrick, D. E. Stevens, and O. B. Toon (2004), The impact of humidity above stratiform clouds on indirect climate forcing, *Nature*, *432*, 1014–1017.

Albrecht, B. A. (1989), Aerosols, cloud microphysics, and fractional cloudiness, *Science*, *245*, 1227–1230.

Barrie, L. A. (1986), Arctic air pollution: an overview of current knowledge, *Atmos. Environ.*, *19*, 1995–2010.

Borys, R. D. (1989), Studies of ice nucleation by arctic aerosol on AGASP-II, *J. Atmos. Chem.*, *9*, 169–185.

Borys, R. D., D. H. Lowenthal, and D. L. Mitchell (2000), The relationships among cloud microphysics, chemistry, and precipitation rate in cold mountain clouds, *Atmos. Environ.*, *34*, 2593–2602.

Borys, R. D., D. H. Lowenthal, S. A. Cohn, and W. O. J. Brown (2003), Mountaintop and radar measurements of anthropogenic aerosol effects on snow growth and snowfall rate, *Geophys. Res. Lett.*, *30*(10), 1538, doi:10.1029/2002GL016855.

Briegleb, B. (1992a), Delta-Eddington approximation for solar radiation in the NCAR Community Climate Model, *J. Geophys. Res.*, *97*, 7603–7612.

Briegleb, B. (1992b), Longwave band model for thermal radiation in climate studies, *J. Geophys. Res.*, *97*, 11,475–11,485.

Bromwich, D. H., J. J. Cassano, T. Klein, T. G. Heinemann, K. M. Hines, K. Steffen, and J. E. Box (2001), Mesoscale modeling of katabatic winds

over Greenland with the Polar MM5, *Mon. Weather Rev.*, *129*, 2290–2309.
Curry, J. A. (1995), Interactions among aerosols, clouds, and climate of the Arctic Ocean, *Sci. Total Environ.*, *160*, 777–791.
Curry, J. A., and E. E. Ebert (1990), Sensitivity of the thickness of Arctic sea ice to the optical properties of clouds, *Ann. Glaciol.*, *14*, 43–46.
Curry, J. A., J. L. Schramm, and E. E. Ebert (1993), Impact of clouds on the surface radiation balance of the Arctic Ocean, *Meteorol. Atmos. Phys.*, *51*, 197–217.
Curry, J. A., W. B. Rossow, and J. L. Schramm (1996), Overview of arctic cloud and radiation properties, *J. Clim.*, *9*, 1731–1764.
Curry, J. A., et al. (2000), FIRE Arctic clouds experiment, *Bull. Am. Meteorol. Soc.*, *81*, 5–29.
Curry, J. A., J. Maslanik, G. Holland, and J. O. Pinto (2004), Application of Aerosondes in the Arctic, *Bull. Am. Meteorol. Soc.*, *85*, 1855–1861.
Ebert, E. E., and J. A. Curry (1992), A parameterization of ice-cloud optical properties for climate models, *J. Geophys. Res.*, *97*, 3831–3836.
Fridlind, A. M., M. Jacobson, V.-M. Kerminen, R. E. Hillamo, V. Ricrad, and J.-L. Jaffrezo (2000), Analysis of gas-aerosol partitioning in the Arctic: Composition of size-resolved equilibrium model results with field data, *J. Geophys. Res.*, *105*, 19,891–19,904.
Fridlind, A. M., A. S. Ackerman, G. McFarquhar, G. Zhang, M. R. Poellot, P. J. DeMott, A. J. Prenni, and A. J. Heymsfield (2007), Ice properties of single-layer stratocumulus during the Mixed-Phase Arctic Cloud Experiment (M-PACE): 2. Model results, *J. Geophys. Res.*, 112, D24202, doi:10.1029/2007JD008646.
Fu, Q. (1996), An accurate parameterization of the solar radiative properties of cirrus clouds, *J. Clim.*, *9*, 2058–2082.
Garrett, T. J., L. F. Radke, and P. V. Hobbs (2002), Aerosol effects on cloud emissivity and surface longwave heating in the Arctic, *J. Atmos. Sci.*, *59*, 769–778.
Garrett, T. J., and C. Zhou (2006), Increased longwave Arctic cloud emissivity associated with pollution from mid-latitudes, *Nature*, *440*, 787–789.
Ghan, S. J., L. R. Leung, and R. C. Easter (1997), Predictgion of cloud droplet number in a general circulation model, *J. Geophys. Res.*, *102*, 21,777–21,794.
Grell, G. A., J. Dudhia, and D. R. Stauffer (1994), A description of the Fifth-Generation Penn State/NCAR Mesoscale Model (MM5), *NCAR Tech. Note NCAR/TN-398 + STR*, 138 pp.
Harrington, J. Y., T. Reisen, W. R. Cotton, and S. M. Kreidenweis (1999), Cloud resolving simulations of Arctic stratus. Part II: Transition-season clouds, *Atmos. Res.*, *51*, 45–75.
Hallett, J., and S. C. Mossop (1974), Production of secondary ice particles during the riming process, *Nature*, *249*, 26–28.
Holland, G. J., P. J. Webster, J. A. Curry, G. Tyrell, D. Auntlett, G. Brett, J. Becker, R. Hoag, and W. Vaglienti (2001), The Aerosonde robotic aircraft: A new paradigm for environmental observations, *Bull. Am. Meteorol. Soc.*, *82*, 889–901.
Houghton, J. T., Y. Ding, D. J. Griggs, M. Noguer, P. J. van der Linden, and D. Xiasu (Eds.) (2001), *Climate Change 2001: The Scientific Basis*, Cambridge Univ. Press, 944 pp.
Ikawa, M., and K. Saito (1990), Description of the nonhydrostatic model developed at the Forecast Research Department of the MRI, *Meteorological Institute Tech. Rep.*, *28*, 238 pp.
Intrieri, J. M., M. D. Shupe, T. Uttal, and B. J. McCarty (2002), An annual cycle of Arctic cloud characteristics observed by radar and lidar at SHEBA, *J. Geophys. Res.*, 107(C10), 8029, doi:10.1029/2000JC000423.
Janjic, Z. I. (1994), The step-mountain Eta coordinate model: Further developments of the convection, viscous layer, and turbulence closure schemes, *Mon. Weather Rev.*, *122*, 927–945.
Jiang, H., W. R. Cotton, J. O. Pinto, J. A. Curry, and M. J. Weissbluth (2000), Cloud resolving simulations of mixed-phase arctic stratus observed during BASE: Sensitivity to concentration of ice crystals and large-scale heat and moisture advection, *J. Atmos. Sci.*, *57*, 2105–2117.
Liu, X., J. E. Penner, S. J. Ghan, and M. Wang (2007), Inclusion of ice microphysics in the NCAR Community Atmosphere Model Version 3 (CAM3), *J. Clim.*, (in press).
Locatelli, J. D., and P. V. Hobbs (1974), Fallspeeds and masses of solid precipitation particles, *J. Geophys. Res.*, *79*, 2185–2197.
Lohmann, U. (2002), Possible effects on ice clouds via contact nucleation, *J. Atmos. Sci.*, *59*, 647–656.
Lohmann, U., J. Feichter, C. C. Chuang, and J. E. Penner (1999), Prediction of the number of cloud droplets in the ECHAM GCM, *J. Geophys. Res.*, *104*, 9169–9198.
Lohmann, U., J. Zhang, and J. Pi (2003), Sensitivity studies of the effect of increased aerosol concentrations and snow crystal shape on the snowfall rate in the Arctic, *J. Geophys. Res.*, *108*(D11), 4341, doi:10.1029/2003JD003377.
Long, C. N., and Y. Shi (2006), The QCRad Value Added Product: Surface radiation measurement quality control testing, including climatologically configurable limits, *Atmospheric Radiation Measurement Program Technical Report, ARM TR-074*, 69 pp.
Lubin, D., and A. M. Vogelmann (2006), A climatologically significant aerosol longwave indirect effect in the Arctic, *Nature*, *439*, 453–456.
McFarquhar, G. M., G. Zhang, M. Poellot, J. Verlinde, G. Kok, R. McCoy, T. Tooman, A. Fridlind, and A. J. Heymsfield (2007), Ice properties of single layer boundary clouds during the Mixed-Phase Arctic Cloud Experiment (MPACE): Part I Observations, *J. Atmos. Sci*.
Meyers, M. P., P. J. DeMott, and W. R. Cotton (1992), New primary ice nucleation parameterization in an explicit model, *J. Appl. Meteorol.*, *31*, 708–721.
Morrison, H., and W. W. Grabowski (2006), Comparison of bulk and bin warm rain microphysics models using a kinematic framework, *J. Atmos. Sci.*, *64*, 2839–2861.
Morrison, H., and J. O. Pinto (2005), Mesoscale modeling of springtime arctic mixed-phase stratiform clouds using a new two-moment bulk microphysics scheme, *J. Atmos. Sci.*, *62*, 3683–3704.
Morrison, H., and J. O. Pinto (2006), Intercomparison of bulk cloud microphysics schemes in mesoscale simulations of springtime arctic mixed-phase stratiform clouds, *Mon. Wea. Rev.*, *134*, 1880–1900.
Morrison, H., J. A. Curry, and V. I. Khvorostyanov (2005a), A new double-moment microphysics scheme for application in cloud and climate models. Part I: Description, *J. Atmos. Sci.*, *62*, 1665–1677.
Morrison, H., J. A. Curry, M. D. Shupe, and P. Zuidema (2005b), A new double-moment microphysics scheme for application in cloud and climate models. Part II: Single-column modeling of Arctic clouds, *J. Atmos. Sci.*, *62*, 1678–1693.
Morrison, H., M. D. Shupe, J. O. Pinto, and J. A. Curry (2005c), Possible roles of ice nucleation mode and ice nuclei depletion in the extended lifetime of arctic mixed-phase clouds, *Geophys. Res. Lett.*, *32*, L18801, doi:10.1029/2005GL023614.
Pinto, J. O. (1998), Autumnal mixed-phase cloudy boundary layers in the Arctic, *J. Atmos. Sci.*, *55*, 2016–2038.
Pinto, J. O., J. A. Curry, and J. M. Intrieri (2001), Cloud-aerosol interactions during autumn over the Beaufort Sea, *J. Geophys. Res.*, *106*, 15,077–15,097.
Prenni, A. J., J. Y. Harrington, M. Tjernstrom, P. J. DeMott, A. Avramov, C. N. Long, S. M. Kreidenweis, P. Q. Olsson, and J. Verlinde (2007), Can ice-nucleating aerosols affect Arctic seasonal climate?, *Bull. Am. Meterol. Soc.*, 541–550.
Pruppacher, H. R., and J. D. Klett (1997), *Microphysics of Clouds and Precipitation*, Kluwer Academic, 954 pp.
Rogers, D. C., P. J. DeMott, S. M. Kreidenweis, and Y. Chen (2001a), A continuous-flow diffusion chamber for airborne measurements of ice nuclei, *J. Atmos. Ocean. Tech.*, *18*, 725–741.
Rogers, D. C., P. J. DeMott, and S. M. Kreidenweis (2001b), Airborne measurements of tropospheric ice nucleating aerosol particles in the Arctic spring, *J. Geophys. Res.*, *106*, 15,053–15,063.
Saleeby, S. M., and W. R. Cotton (2004), A large-droplet mode and prognostic number concentration of clouds droplets in the Colorado State University Regional Atmospheric Modeling System (RAMS). Part I: Module descriptions and supercell test simulations, *J. Appl. Meteor.*, *43*, 182–195.
Savijarvi, H., and P. Raisanen (1998), Long-wave optical properties of water clouds and rain, *Tellus(A)*, *50*, 1–11.
Schnell, R. C. (1977), Ice nuclei in seawater, fog water and marine air off the coast of Nova Scotia: Summer 1975, *J. Atmos. Sci.*, *34*, 1299–1305.
Shaw, G. E. (1986), Aerosols in Alaskan air masses, *J. Atmos. Chem.*, *4*, 157–171.
Shupe, M. D., and J. M. Intrieri (2004), Cloud radiative forcing of the Arctic surface: The influence of cloud properties, surface albedo, and solar zenith angle, *J. Clim.*, *17*, 616–628.
Sirois, A., and L. A. Barrie (1999), Arctic lower tropospheric aerosol trends and composition at Alert, Canada: 1980–1995, *J. Geophys. Res.*, *104*, 11,599–11,618.
Slingo, A. (1989), A GCM parameterization for the shortwave optical properties of water clouds, *J. Atmos. Sci.*, *46*, 1419–1427.
Stephens, G. L. (2005), Cloud feedbacks in the climate system: A critical review, *J. Clim.*, *18*, 237–273.
Thompson, G., R. M. Rasmussen, and K. Manning (2004), Explicit forecasts of winter precipitation using an improved bulk microphysics scheme. Part I: Description and sensitivity analysis, *Mon. Weather Rev.*, *132*, 519–542.
Turner, D. D., S. A. Clough, J. C. Liljegren, E. E. Clothiax, K. Cady-Pereira, and K. L. Gaustad (2006), Retrieving liquid water path and precipitable water vapor from the Atmospheric Radiation Measurement

(ARM) microwave radiometers, *IEEE Trans. Geosci. Remote Sens.*, (accepted).

Twomey, S. (1977), The influence of pollution on the shortwave albedo of clouds, *J. Atmos. Sci.*, *34*, 1149–1152.

Verlinde, J., et al. (2007), Overview of the Mixed-Phase Arctic Cloud Experiment (MPACE), *Bull. Amer. Meteorol. Soc*, (in press).

Yang, D. (1999), An improved precipitation climatology for the Arctic Ocean, *Geophys. Res. Lett.*, *26*(11), 1625–1628.

Yum, S. S., and J. G. Hudson (2001), Vertical distribution of cloud condensation nuclei spectra over the springtime Arctic Ocean, *J. Geophys. Res.*, *106*, 15,045–15,052.

Zhou, J., E. Swietlicki, O. H. Berg, P. P. Aalto, K. Hameri, E. D. Nilsson, and C. Leck (2001), Hygroscopic properties of aerosol particles over the central Arctic Ocean during summer, *J. Geophys. Res.*, *106*, 32,111–32,123.

Zuidema, P., et al. (2005), An arctic springtime mixed-phase cloudy boundary layer observed during SHEBA, *J. Atmos. Sci.*, *62*, 160–176.

J. A. Curry, School of Earth and Atmospheric Science, Georgia Institute of Technology, Atlanta, GA, USA.

G. M. McFarquhar, University of Illinois, Urbana, IL, USA.

H. Morrison and J. O. Pinto, National Center for Atmospheric Research, P. O. Box 3000, Boulder, CO 80309, USA. (morrison@ucar.edu)